



Fabrication of perovskite-type macro/mesoporous $\text{La}_{1-x}\text{K}_x\text{FeO}_{3-\delta}$ nanotubes as an efficient catalyst for soot combustion

Fan Fang, Nengjie Feng, Lei Wang, Jie Meng, Geng Liu, Peng Zhao, Pengfei Gao, Jing Ding, Hui Wan*, Guofeng Guan*

State Key Laboratory of Materials-Oriented Chemical Engineering, College of Chemical Engineering, Jiangsu National Synergetic Innovation Center for Advanced Materials, Nanjing Tech University, Nanjing 210009, PR China



ARTICLE INFO

Keywords:

Electrospinning
Perovskite
 K^+ doping
Macro/mesoporous tubular structure
Soot combustion

ABSTRACT

Perovskite-type macro/mesoporous nanotube shows large specific surface area and high utilization of catalytic sites, which gives rise to the enhancement of catalytic activity and broaden their application. In this work, perovskite-type $\text{La}_{1-x}\text{K}_x\text{FeO}_{3-\delta}$ nanotubes were prepared for efficient soot oxidation by a simple electrospinning technique following calcination. The as-prepared samples were characterized by XRD, FI-IR, FE-SEM, TEM, XPS, N_2 adsorption-desorption, H_2 -TPR and O_2 -TPD techniques to investigate the physical-chemical properties. A certain amount of K^+ doped in to $\text{LaFeO}_{3-\delta}$ nanotubes sample could inhibit the growth of crystallites during the calcination at a high temperature, which could prevent the destruction of macro/mesoporous tubular structure and contribute to the more contact between soot particles and active sites. Meanwhile, it could also bring about the higher oxygen vacancy density responsible for the enhancement of redox abilities. However, excessive doping of K^+ could lead to the collapsing of macro/mesoporous tubular structure, ascribable to the formation of low-melting compounds or eutectics with other components of the catalyst, which would have a negative influence on the catalytic performance. The performance for soot catalytic oxidation was evaluated in a temperature programmed oxidation device using O_2 (without or with NO) as oxidant. Among the as-prepared catalysts, the well-structured $\text{La}_{0.8}\text{K}_{0.2}\text{FeO}_{3-\delta}$ nanotubes catalyst is the best candidate for soot removal.

1. Introduction

As known, diesel engines have been widely used in various areas for their less carbon dioxide emissions, higher fuel efficiency and good economy [1]. However, particulate matter (PM) in diesel combustion process has attracted more and more attention, because it can give rise to serious environmental and health problems [2–5]. At present, the PM is commonly controlled by the diesel particulate filter (DPF) systems, which can capture the soot physically with no catalytic processes [6]. However, they require a regeneration system coordinating with the DPF system like other filters to eliminate the accumulated PM [7], in order to continuously maintain the performance of filter [8]. To resolve this problem, some works about regeneration methods have been conducted by the researchers, but the results are not perfectly satisfactory. For example, it has been reported to regenerate the filter with nitrogen dioxide [9]. However, it needs sufficient nitrogen dioxide for effective regeneration while it can't be achieved under normal combustion operating conditions. In addition, methods involving in oxidizing PM directly for generation have been studied. But they all need a high

temperature above 600 °C which can result in the destruction of the DPF. To overcome these limitations, the catalytic combustion technique combined with DPFs is widely employed for its efficient soot removal through a relatively complex gas-solid-solid reaction [10]. Therefore, the oxidation catalysts play an important role in the after-treatment technique [11]. Up to now, many kinds of catalysts have been studied and employed for soot effective oxidation, such as alkaline and alkaline-earth metal oxides [12], precious metals [13], spinel [14] and perovskite-type oxides [15–17]. Among them, perovskite-type oxides have been widely used as promising catalysts for soot oxidation, mainly owing to their higher chemical/thermal/structural stability than the alkaline and alkaline-earth metal oxides, relatively lower cost than the precious metals and high oxidation activity [18].

It has been widely known that ABO_3 is the general formula for perovskite-type oxides. Rare earth metal elements are commonly at the A site which plays an important role in stabilizing the structure of perovskite. In addition, transition metal elements are commonly at the B site as the active center related to the catalytic activity. For this type of catalyst, active oxygen species can be seen as the source of the oxidizing

* Corresponding authors.

E-mail addresses: wanhui@njtech.edu.cn (H. Wan), njutggf@163.com (G. Guan).

capability, which are the key to enhancing the oxidation activity. LaFeO₃ has potential applications in redox reactions due to its exceeding properties, such as cheapness and high stability [19]. Although LaFeO₃ are not the most active perovskite-type materials for catalytic soot oxidation, they exhibit improved resistance against high temperature and redox treatments, which promotes them to be interesting materials for diesel particulate after-treatment [20]. At present, introducing oxygen vacancies in the perovskite lattice has been confirmed as an effective way to obtain higher concentrations of active oxygen species [21]. For example, when the trivalent cations La³⁺ at A site of LaCoO₃ are substituted by univalent cations K⁺, the valence of cations at B site will change accompanied by the formation of oxygen vacancies, improving the mobility of lattice oxygen and the desorption of oxygen species [22]. Furthermore, the structure of the catalyst is also important for the catalytic activity.

Last few years, various of perovskite-type oxides materials with different structures and morphologies were successfully fabricated by different methods, such as the 3DOM (three-dimensionally ordered macroporous) perovskite-type oxides [22,23], 3D (three-dimensional) arrangements of perovskite-type nano-fiber webs [16,24]. They were widely studied and employed for soot catalytic oxidation due to the presence of macropores. As known, the average sizes of macropores in the above structures are far larger than the soot particle size which could give more contact chances between catalysts and soot. So, it is believed that the catalytic activity of the catalysts for soot combustion can be remarkably improved through reasonable design on the morphology of catalysts. On the basis of this idea, the perovskite-type porous nanotubes could be designed as a potential catalyst for catalytic soot oxidation considering the following advantages compared with perovskite-type bulks: (i) higher surface specific areas with both macropores and mesopores which could provide more contact for soot-catalyst. (ii) more pathways for soot particles transporting into the nanotube. (iii) more contact with active sites on the inner surface through multiple collisions for the entered soot particles, due to the Brownian-like movement in the reaction gas flow with high space velocity [25]. The perovskite-type nanotubes could be prepared using a simple electrospinning technique. However, the porous tubular structure might be destroyed when calcinated at a high temperature due to the growing up of crystallite size. It has been reported by Jimmy C. Yu and Xianluo Hu groups that the nanofibers with diameters of 50–100 nm can be obtained at 600 °C. If the annealing temperature was continuously increased to 700 °C, the fibrous architecture collapsed into numerous rod-like particles ascribable to the growth of crystallite. However, the morphology of the nanofibers disappeared at 800 °C, and transformed completely into nanoplates with an average thickness of about 50 nm [26]. Therefore, the crystallite size was essential to keep the tubular structure during the calcination. Moreover, for the tubular structure, the hierarchical pores formed on a basis of phase separation in electrospun polymer fibers such as PNA, PS and PMMA [27,28], which needed a solvent with a higher boiling point solvent while hierarchical pores were disappeared using ethanol as solvent in some works [29]. To sum up, the perovskite-type porous nanotubes could be the good potential catalyst for soot combustion, but the preparation for porous nanotubes was relatively difficult.

In this work, we prepared a series of La_{1-x}K_xFeO_{3-δ} perovskite-type nanotubes with macropores and mesopores by a simple electrospinning technique following calcination under same experimental conditions. The metal nitrates and high polymers were dissolved in a mixed solvent, the homogeneous mixtures then were electrospun to nanofibers, and calcined in the air at last (Fig. 1). The as-prepared samples were characterized by XRD, FI-IR, FE-SEM, TEM, XPS, N₂ adsorption-desorption, H₂-TPR and O₂-TPD techniques to investigate the effect of the introduction amount of K⁺ on the morphology, structure and redox abilities of the catalysts. The composite influences of K⁺ introduction with the macro/mesoporous tubular structure on the catalytic soot oxidation were also evaluated by a temperature programmed device

and discussed in detail. Furthermore, to certify the superiority of perovskite-type nanotubes in soot catalytic activity, we also prepared a series of La_{1-x}K_xFeO_{3-δ} (x = 0, 0.1, 0.2, 0.3) perovskite bulks for comparison of the catalytic performance.

2. Experimental section

2.1. Materials

Lanthanum nitrate hexahydrate (La(NO₃)₃·6H₂O, ≥99.9% purity), Polyvinylpyrrolidone (PVP, ≥99.9% purity, M_w ≈ 1,300,000), N,N-dimethylformamide (DMF, AR), Deionized water were purchased from Aladdin Reagent (Aladdin Industrial Corporation). Potassium nitrate (KNO₃, ≥99.9% purity), Iron nitrate nonahydrate (Fe(NO₃)₃·9H₂O, ≥99.9% purity) were obtained from Sinophram Chemical Reagent Co., Ltd. (China).

2.2. Catalyst preparation

Perovskite-type composite oxides nanotubes La_{1-x}K_xFeO_{3-δ} (x = 0, 0.1, 0.2, 0.3) were fabricated by a combination of electrospinning method and sol-gel method followed by subsequent calcination. Above-mentioned metal nitrates were dissolved in a mixed solution of deionized water and dimethylformamide (DMF) in stoichiometric ratios (La_{1-x}K_xFeO₃, x = 0, 0.1, 0.2, 0.3), and the weight ratio of two solvents was 2:8. Here, the weight ratio of total metal nitrates to mixed solvent was 1:6. After vigorously stirred at room temperature for 3 h, PVP were added in it at a weight ratio of 1:1.5 of PVP and metal nitrates, which were used as guide agent and viscosity controller for the formation of uniform nanostructure. Then a stable homogeneous sol gel as precursor was obtained with another 12 h of vigorous stirring at room temperature. Next, the mixtures precursor was transferred to a 5 ml plastic syringe attached to a 27 G (0.21 mm inner diameter) stainless steel needle. The needle was applied by a voltage of 18 kV, and the feed flow was 0.5 mL h⁻¹. The nanofibers were collected by the aluminum foil wrapped in a drum collector which was constantly rotated at a speed of 140 rpm (revolution per minute), and the distance between the needle tip and collector was 15 cm. All the processes of electrospinning were operated at approximately 40 °C and humidity below 35% RH. Subsequently the obtained nanofibers were calcined at 700 °C for 2 h with a program heating rate of 1 °C/min. In this work, the prepared nanotubes with different stoichiometric ratios (x = 0–0.3) were denoted as LaFeO_{3-δ} nanotubes, La_{0.9}K_{0.1}FeO_{3-δ} nanotubes, La_{0.8}K_{0.2}FeO_{3-δ} nanotubes and La_{0.7}K_{0.3}FeO_{3-δ} nanotubes.

As a comparison, catalysts with corresponding stoichiometric ratios were prepared by citrate method. La(NO₃)₃·6H₂O, KNO₃, Fe (NO₃)₃·9H₂O and citric acid were dissolved in deionized water at a molar ratio of 1.1:1 of citric acid and total metal ions. The mixed solution was vigorously stirred at 90 °C until forming sol-gel. After that, the obtained mixtures were further dried at 110 °C overnight and sintered at 700 °C for 2 h with the same way of heating. These catalysts were denoted as LaFeO_{3-δ} bulks, La_{0.9}K_{0.1}FeO_{3-δ} bulks, La_{0.8}K_{0.2}FeO_{3-δ} bulks and La_{0.7}K_{0.3}FeO_{3-δ} bulks.

2.3. Catalyst characterization

X-ray diffraction (XRD) patterns were measured at 100 mA and 40 kV with a Smartlab diffractometer (RIGAKU, Japan) using Cu-K α radiation ($\lambda = 0.1541$ nm). At a scanning range of 20 from 20° to 80°, the intensity of peaks was recorded with a speed of 10° min⁻¹. The morphologies and structures of samples were analyzed using field-emission scanning electron microscopy (FESEM, Hitachi S4800) at 10 kV. The transmission electron microscopy (TEM) was used to further study the internal morphologies and structures (JEOL JEM-2100). The surface area was determined by Brunauer-Emmett-Tell (BET) method and pore size distribution was figured by Barret-Joyner-Halenda (BJH)

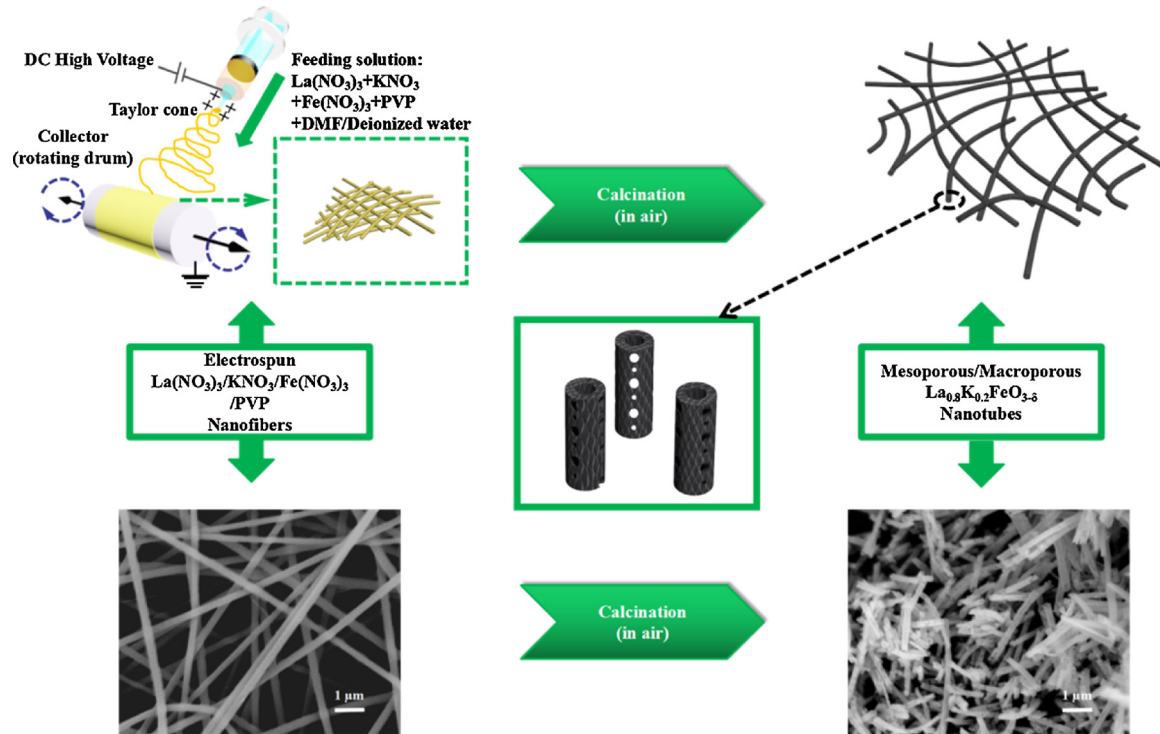


Fig. 1. Schematic illustration of the synthetic strategy of hierarchical maro/mesoporous $\text{La}_{0.8}\text{K}_{0.2}\text{FeO}_{3-\delta}$ nanotubular catalyst.

method. Fourier transform infrared (FT-IR) spectroscopy from 400 to 1200 cm^{-1} was acquired by Thermo Nicolet 870 spectrophotometer using anhydrous KBr as a dispersing agent. Nitrogen adsorption-desorption measurements were conducted on a Micromeritics ASAP 2020 system model apparatus at $-196\text{ }^\circ\text{C}$ after degassed for 4 h in a vacuum at $200\text{ }^\circ\text{C}$. XPS spectra were collected by a PHI 5000 Versa Probe system using monochromatic Al K radiation (1486.6 eV) with an accelerating power of 15 kW. Temperature-programmed reduction (TPR) analysis with H_2 was performed using a chemical adsorption analysis apparatus (Micromeritics AutoChem II 2920). Before the measurement, 30 mg of samples with the size from 40 to 60 meshes were collected and calcined for 2 h at $200\text{ }^\circ\text{C}$. After cooled to room temperature, the catalyst bed was heated to $900\text{ }^\circ\text{C}$ at the rate of $10\text{ }^\circ\text{C min}^{-1}$ with a continuous 10% H_2/Ar flow (50 mL min^{-1}). O_2 -temperature-programmed desorption (O_2 -TPD) was also conducted on a Micromeritics AutoChem II 2920 chemical adsorption analyser. Before the measurement, 50 mg samples (40–60 mesh) was pretreated in Ar stream at $200\text{ }^\circ\text{C}$ for 2 h, and then cooled down to room temperature. Then, O_2 was absorbed at $70\text{ }^\circ\text{C}$ for 2 h in a mixture gas of 3% O_2/Ar , and subsequently the sample was purged by a flowing pure He stream to remove excessive and weakly adsorbed O_2 . Finally, the sample was heated to $900\text{ }^\circ\text{C}$ with a heating rate of $10\text{ }^\circ\text{C/min}$ in a pure He flow and the desorption pattern was recorded.

2.4. Soot oxidation measurements

To evaluate the activity of catalysts, 45 mg catalyst and 5 mg carbon black (Printex-U from Degussa), as a simulated soot substance, were mixed using a spatula and an agate mortar for 10 min under loose contact (LC) model [6]. Temperature programmed oxidation for the catalyst-soot mixture was conducted in a fixed-bed reactor using a quartz tube (inner diameter = 6 mm). The mixture of catalyst and soot were heated from $200\text{ }^\circ\text{C}$ to $700\text{ }^\circ\text{C}$ at a rate of $5\text{ }^\circ\text{C min}^{-1}$ with a 100 mL min^{-1} gas flow of 20% O_2 and 6% H_2O (or without H_2O). The activity of the samples was also studied for the soot combustion with NO/O_2 by feeding O_2 (20%) and NO (500 ppm) under the same test conditions. The concentration of CO_2 in outlet gas was measured using

an infrared gas analysis apparatus (Infralyt 50). The measured values in this work for evaluating the catalytic performance of catalysts were the following: (I) the temperature when the conversion rate of soot reached 10% (T_{10}), (II) the temperature when the conversion rate of soot reached 50% (T_{50}), (III) the temperature when the conversion rate of soot reached 90% (T_{90}), (IV) the selectivity for CO_2 at the temperature of highest soot burning rate ($S_{\text{CO}_2}^m$).

The isothermal reactions were also conducted for the kinetic analysis of soot combustion, at which a stable and an appropriate conversion of soot (less than 15%) was achieved in an approximate kinetic regime. The selection of $320\text{ }^\circ\text{C}$ was made due to that the soot conversion was low and the soot conversion was nearly constant overtime. The soot conversion increased significantly above $320\text{ }^\circ\text{C}$ and the reaction could not be thought to be in a stable state. The total flow rate was 150 ml/min, which could avoid the external mass transport limitations [30]. Thus the turnover numbers (TON) and the reaction rate, turnover frequency (TOF) could be obtained. TON [31,32] and TOF [33,34] are both useful to study the activity of the catalyst. Among them, TON_K and TOF_K were on the basis of the K-doping amount.

3. Results and discussion

3.1. Characterization of $\text{La}_{1-x}\text{K}_x\text{FeO}_{3-\delta}$ perovskite nanotubes

To determine the phase structures of the $\text{LaFeO}_{3-\delta}$ nanotubes, $\text{La}_{0.9}\text{K}_{0.1}\text{FeO}_{3-\delta}$ nanotubes, $\text{La}_{0.8}\text{K}_{0.2}\text{FeO}_{3-\delta}$ nanotubes and $\text{La}_{0.7}\text{K}_{0.3}\text{FeO}_{3-\delta}$ nanotubes, all the catalysts were examined by XRD (Fig. 2). As shown in Fig. 2a, the measured XRD patterns of the samples showed the major diffraction peaks with 2θ at 22.61 , 32.19 , 39.67 , 46.14 , 52.00 , 57.40 , 67.35 and 76.64° correspond to (101), (121), (220), (202), (141), (240), (242) and (204) lattice faces, which clearly illustrated the presence of orthorhombic phased LaFeO_3 (JCPDS No. 37-1493). The magnified XRD patterns shown in Fig. 2b given more information about (121) lattice face and d value for different amount of K⁺ doping in A site. The angles of the (121) reflection are 32.20 , 32.24 , 32.30 and 32.30° which are correspond to $\text{LaFeO}_{3-\delta}$, $\text{La}_{0.9}\text{K}_{0.1}\text{FeO}_{3-\delta}$, $\text{La}_{0.8}\text{K}_{0.2}\text{FeO}_{3-\delta}$ and $\text{La}_{0.7}\text{K}_{0.3}\text{FeO}_{3-\delta}$ nanotubes. In addition, the d values

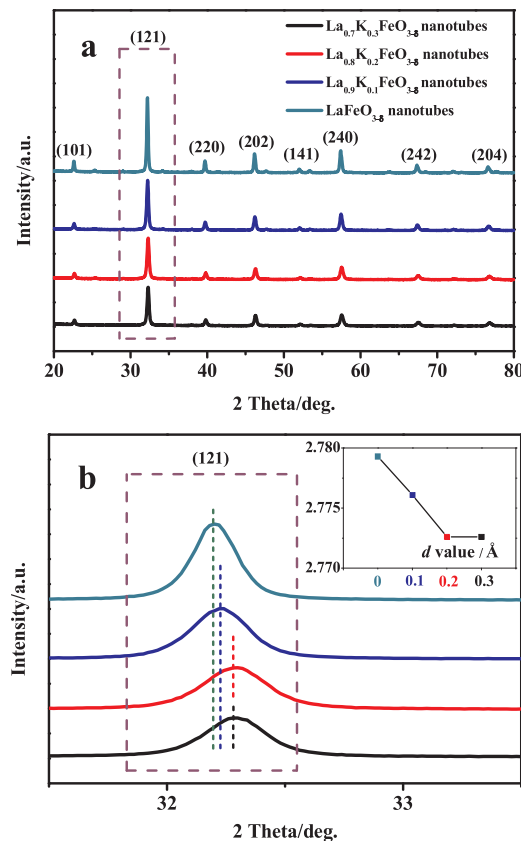


Fig. 2. XRD patterns of $\text{La}_{1-x}\text{K}_x\text{FeO}_{3-\delta}$ ($x = 0, 0.1, 0.2$ and 0.3) perovskite-type nanotubes.

(basal spacing) of the (121) lattice are 2.7776 , 2.7743 , 2.7693 and 2.7693 \AA , respectively. It could be easily summarized from above that with the increase of K^+ doping, the (121) reflection angles offset to higher angles while the d values decreased. Furthermore, the peak becomes smaller as the K^+ doping increase and the b axis cell parameters in (121) lattice faces change from 7.8600 to 7.8548 , 7.8491 and 7.8365 \AA indicated in Supplementary Table S1. These changes are mainly due to the different crystal ionic radii by partial substitution of La^{3+} with K^+ ion in the A site [16], as the K^+ ion has a larger ionic diameter than La^{3+} ion ($\text{La}^{3+}:0.106\text{ nm}$, $\text{K}^+:0.133\text{ nm}$).

Fig. S3 shows the FT-IR spectra of the $\text{La}_{1-x}\text{K}_x\text{FeO}_3$ ($x = 0-0.4$) nanotubes, which can further reveal the phase composition. All $\text{La}_{1-x}\text{K}_x\text{FeO}_3$ samples have an IR absorption band at around 443 cm^{-1} , which may be attributed to O–Fe–O deformation vibration, and the strong absorption band at around 581 cm^{-1} is attributed to the asymmetrical stretching vibration band of the Fe–O in FeO_6 octahedrons [23]. A shoulder peak appears at around 646 cm^{-1} indicating the low-symmetry structure, which is consistent with the orthorhombic structure confirmed by XRD [35]. These results further certificate that the perovskite oxides are formed. Meanwhile, it can be observed that the peaks become weaker and broader, which is caused by the charge imbalance arising from the replacement of La^{3+} by K^+ . Therefore, some oxygen vacancies will appear in the perovskite unit and the oxygen activity of the $\text{La}_{1-x}\text{K}_x\text{FeO}_{3-\delta}$ nanotubes catalysts will be improved [23]. In addition, there are no organic residues (PVP) in the fresh catalysts detected by the FT-IR spectra, which suggests the polymers (PVP) have been removed completely after calcined at $700\text{ }^\circ\text{C}$ for 2 h .

Fig. 3 shows the electrospun precursor nanofibers and $\text{La}_{1-x}\text{K}_x\text{FeO}_{3-\delta}$ nanotubes calcined in $700\text{ }^\circ\text{C}$. As shown in the images of electrospun precursor nanofibers with a smooth surface (Fig. 3b, f, j and n), the diameter distributions of the nanofibers are all narrow indicating the nanofibers are very uniform (inset of Fig. 3a, e, i and k). In addition, the

average diameters of nanofibers are 287 , 284 , 288 and 289 nm respectively, which show almost none differences in the average diameter of nanofibers electrospun under the same conditions. It can be obviously seen from the images of nanotubes calcined in $700\text{ }^\circ\text{C}$, only the tubular nanostructures of $\text{La}_{0.9}\text{K}_{0.1}\text{FeO}_{3-\delta}$ and $\text{La}_{0.8}\text{K}_{0.2}\text{FeO}_{3-\delta}$ nanotubes are obtained while the nanostructures of $\text{LaFeO}_{3-\delta}$ and $\text{La}_{0.7}\text{K}_{0.3}\text{FeO}_{3-\delta}$ are destroyed. The average outer diameters of $\text{La}_{0.9}\text{K}_{0.1}\text{FeO}_{3-\delta}$ nanotubes and $\text{La}_{0.8}\text{K}_{0.2}\text{FeO}_{3-\delta}$ nanotubes are respectively around 165 nm and 167 nm both with a uniformly narrow distribution (inset of Fig. 3g and k). Furthermore, some small pores on the surface of $\text{La}_{0.9}\text{K}_{0.1}\text{FeO}_{3-\delta}$ nanotubes and $\text{La}_{0.8}\text{K}_{0.2}\text{FeO}_{3-\delta}$ nanotubes can be observed (inset of Fig. 3h and l), which are caused by the generated gases related to the decomposition of metal nitrates and high polymer during calcination. For $\text{LaFeO}_{3-\delta}$ nanotubes, the tubular structure is destroyed due to the growth of crystallite size when rising the calcination temperature from $600\text{ }^\circ\text{C}$ to $700\text{ }^\circ\text{C}$. The $\text{LaFeO}_{3-\delta}$ nanofibers can be prepared successfully by following calcination at $600\text{ }^\circ\text{C}$, which can be obtained from previous research work [36] and further verified in this work shown in Fig. S4. With the increase of K^+ doping amount ($x = 0, 0.1, 0.2$ and 0.3), the average crystallite size calculated by Scherrer formula changes from 47.0 to 30.8 nm (Table S1 and Fig. S5) and the tubular structures are formed, which is in agreement with the conclusion above. In addition, the structure of $\text{La}_{0.7}\text{K}_{0.3}\text{FeO}_{3-\delta}$ nanotubes is also destroyed with no correlation with the crystallite size, yet. This may be due to the formation of low-melting compounds or eutectics with other components of the catalyst that influence the structure of the nanotube during the heat treatment [37], which can be observed from the decrease of specific surface area with the increase in the K-substituted amount shown in Table 3.

X-ray photoelectron spectroscopic studies were conducted to study the surface element valence and content of La and Fe, as well as the relative content of different surface oxygen species, which play an important role in soot combustion at a low temperature. As shown in Fig. 4a, there are two similar peaks of $\text{La}^{3d_{5/2}}$ and $\text{La}^{3d_{3/2}}$ in the La 3d region. They are referred to the La^{3+} oxide phase ($833.1-833.6\text{ eV}$) and a lower-oxidation state ($837.4-837.9\text{ eV}$) caused by the formation of hydroxylgroup [16], which indicate that the La ions are trivalent in the catalysts. These results prove that there are no effects on the valence state of La on the catalysts surface by the doping of K. Fig. 4b shows the XPS spectra of Fe 2p, there is an asymmetrical $\text{Fe}^{2p_{3/2}}$ XPS signal for each of the samples, which could be divided into two components attributed to the surface Fe^{4+} species at around 711.7 eV and surface Fe^{3+} species at around 709.8 eV [38]. As shown in Table S2, the surface relative percentage of Fe^{3+} to Fe^{4+} decreases in the order of $\text{La}_{0.8}\text{K}_{0.2}\text{FeO}_{3-\delta}$ nanotubes (1.10) $>$ $\text{La}_{0.7}\text{K}_{0.3}\text{FeO}_{3-\delta}$ nanotubes (1.05) $>$ $\text{La}_{0.9}\text{K}_{0.1}\text{FeO}_{3-\delta}$ nanotubes (0.98) $>$ $\text{LaFeO}_{3-\delta}$ nanotubes, which implies the $\text{La}_{0.8}\text{K}_{0.2}\text{FeO}_{3-\delta}$ nanotubes catalyst would possess the highest oxygen vacancy density on the basis of the electroneutrality principle [38]. This phenomenon is further confirmed by the O 1s XPS spectra. It can be seen from the Fig. 4c, the asymmetrical O 1s XPS results could be split into two components for adsorbed oxygen (O_{ads} , O^-) at $531.1-531.4\text{ eV}$ and surface lattice oxygen (O_{lat} , O^{2-}) at $528.7-529.2\text{ eV}$, respectively [16]. It also can be seen in Table 1, the molar ratios of the adsorbed oxygen and the lattice oxygen ($\text{O}_{\text{ads}}/\text{O}_{\text{lat}}$) on the surface of each prepared samples are 0.57 ($\text{LaFeO}_{3-\delta}$ nanotubes), 0.60 ($\text{La}_{0.9}\text{K}_{0.1}\text{FeO}_{3-\delta}$ nanotubes), 0.76 ($\text{La}_{0.8}\text{K}_{0.2}\text{FeO}_{3-\delta}$ nanotubes) and 0.75 ($\text{La}_{0.7}\text{K}_{0.3}\text{FeO}_{3-\delta}$ nanotubes). They are in the sequence of $\text{La}_{0.8}\text{K}_{0.2}\text{FeO}_{3-\delta}$ nanotubes $>$ $\text{La}_{0.7}\text{K}_{0.3}\text{FeO}_{3-\delta}$ nanotubes $>$ $\text{La}_{0.9}\text{K}_{0.1}\text{FeO}_{3-\delta}$ nanotubes $>$ $\text{LaFeO}_{3-\delta}$ nanotubes. It has been reported that the partial substitutions of La^{3+} by Ca^{2+} in the $\text{La}_{1-x}\text{Ca}_x\text{CoO}_3$ catalysts lead to the increase of oxygen vacancy density [39,40]. Therefore, it is likely that the vacancy oxygen density can be increased by the increase in the K^+ doping level, which is consistent with the Fe 2p_{3/2} results. But for the $\text{La}_{0.7}\text{K}_{0.3}\text{FeO}_{3-\delta}$ nanotubes, the value of $\text{O}_{\text{ads}}/\text{O}_{\text{lat}}$ is slightly smaller compared with $\text{La}_{0.8}\text{K}_{0.2}\text{FeO}_{3-\delta}$ nanotubes, may be due to the part destruction of nanotubular structure.

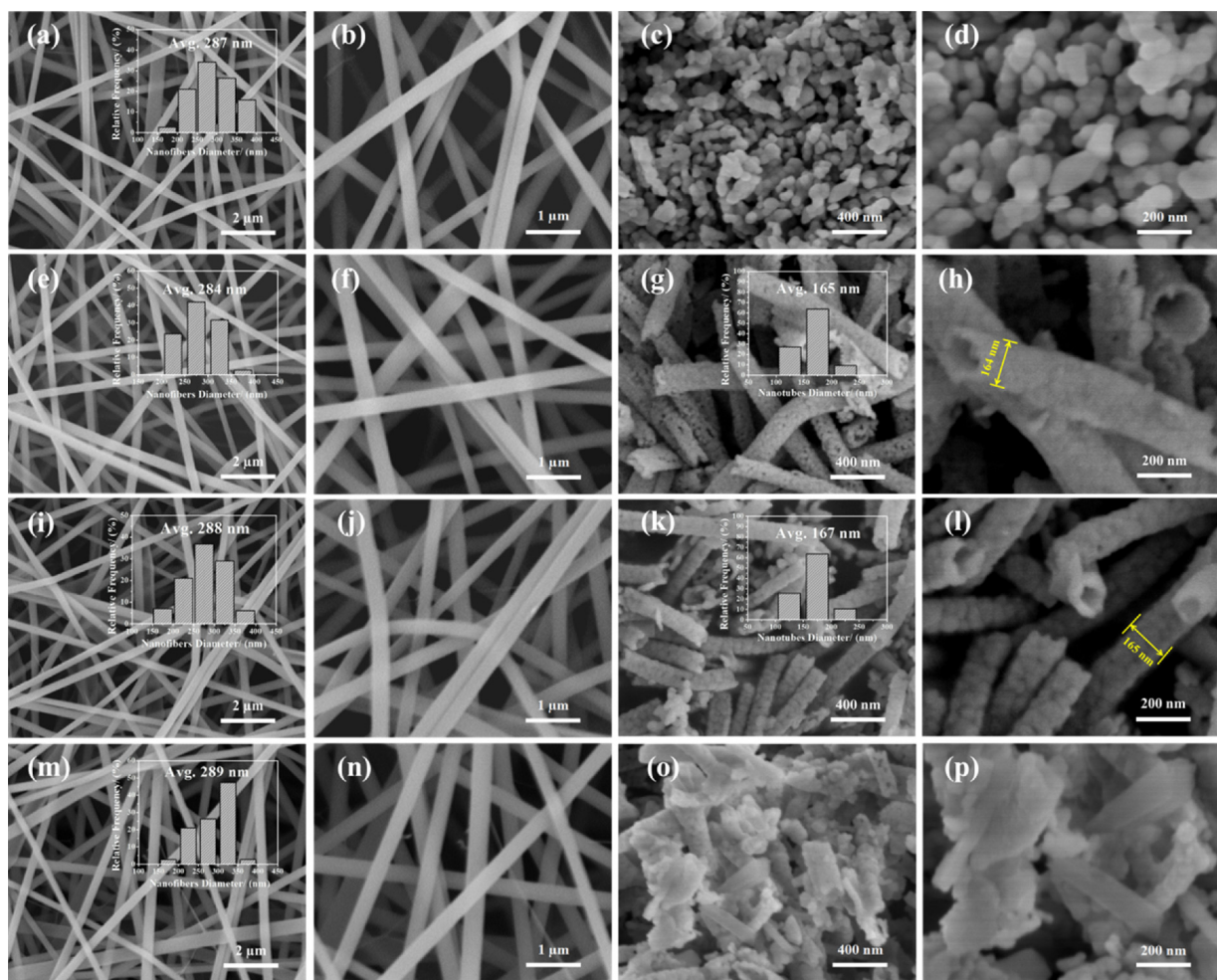


Fig. 3. SEM images of electrospun precursor nanofibers: (a) and (b) $\text{LaFeO}_{3-\delta}$; (e) and (f) $\text{La}_{0.9}\text{K}_{0.1}\text{FeO}_{3-\delta}$; (i) and (j) $\text{La}_{0.8}\text{K}_{0.2}\text{FeO}_{3-\delta}$; (m) and (n) $\text{La}_{0.7}\text{K}_{0.3}\text{FeO}_{3-\delta}$. SEM images of $\text{La}_{1-x}\text{K}_x\text{FeO}_{3-\delta}$ ($x = 0, 0.1, 0.2$ and 0.3) nanotubes: (c) and (d) $x = 0$; (g) and (h) $x = 0.1$; (k) and (l) $x = 0.2$; (o) and (p) $x = 0.3$.

$\text{H}_2\text{-TPR}$ was used to characterize the reducibility of the catalysts, and the TPR profiles were reported in Fig. 5a. All of the catalysts start to reduce at relatively low temperatures whose extent increases strongly with K substitution. The reduction peaks at 355°C , 301°C , 325°C and 334°C in the corresponding catalysts can be attributed to the reduction of Fe^{4+} to Fe^{3+} as well as the removal of a small amount of O_{ads} [38,41]. The intensity of this peak enhances with the increasing amount of K substitution, which indicates that the amounts of the O_{ads} in the surface related to the soot combustion at low temperature. For $\text{La}_{0.7}\text{K}_{0.3}\text{FeO}_{3-\delta}$ nanotubes, the intensity is higher than $\text{La}_{0.8}\text{K}_{0.2}\text{FeO}_{3-\delta}$ nanotubes but the value of $\text{O}_{\text{ads}}/\text{O}_{\text{lat}}$ is smaller. The large reduction peaks between 380°C and 450°C in these catalysts ascribe to the reduction of Fe^{3+} to Fe^{2+} . It moves up to a lower temperature with increasing in K^+ substitution compared with $\text{LaFeO}_{3-\delta}$ nanotubes, suggesting a lower stability of Fe^{3+} in the perovskite structure when La^{3+} is partially replaced by K^+ . The temperature of large reduction peak for $\text{La}_{0.7}\text{K}_{0.3}\text{FeO}_{3-\delta}$ nanotubes is a little higher than $\text{La}_{0.8}\text{K}_{0.2}\text{FeO}_{3-\delta}$ nanotubes, can be attributed to either the lower surface area reducing the H_2 diffusion rate towards the core of catalysts, or to the contribution of some iron oxide presented likely as very small crystallites not detected by XRD analysis, whose reduction temperature is in this range. These similar results are observed in the $\text{La}_{1-x}\text{Ca}_x\text{FeO}_3$ catalysts [41].

O_2 temperature-programmed desorption ($\text{O}_2\text{-TPD}$) measurements were conducted to investigate the capability to activate oxygen, which was related to the catalytic performance of materials for oxidation

reaction. As shown in Fig. 5b, the O_2 desorption peak of $\text{LaFeO}_{3-\delta}$ nanotubes is very weak. However, the $\text{O}_2\text{-TPD}$ profiles of other samples show that there are three oxygen desorption peaks. The first peak in the range of 50°C to 200°C is assigned to the desorption of physical adsorption oxygen species (O_2). The second peak ranging from 200°C to 400°C is assigned to the desorption of chemisorbed surface-active oxygen species (O_2^- , O^-). The third peak above 400°C refers to the desorption of lattice oxygen (O^{2-}) [23]. As known, the activity of soot catalytic oxidation mainly depends on the surface-active oxygen species at a relatively low temperature. Seen from Fig. 5b, it is clear that the intensity of oxygen desorption peak in the range of 200°C to 400°C increases remarkably with increasing K-doping amount, indicating that the K-doping promotes the adsorption and activation of oxygen. However, the surface-active oxygen desorption peak of $\text{La}_{0.7}\text{K}_{0.3}\text{FeO}_{3-\delta}$ nanotubes is lower than $\text{La}_{0.8}\text{K}_{0.2}\text{FeO}_{3-\delta}$ nanotubes due to the destruction of porous nanotubular structure, which implies that the porous nanotubular structure is beneficial to the adsorption and activation of oxygen. The intensity of lattice oxygen (O^{2-}) desorption peak increases with the increasing K-doping amount, which is attributed to the charge imbalance arising from the replacement of La^{3+} by K^+ . This result can be also obtained from the analysis about FT-IR. In summary, the $\text{O}_2\text{-TPD}$ measurements show that the $\text{La}_{0.8}\text{K}_{0.2}\text{FeO}_{3-\delta}$ nanotubes possesses the highest amount of chemisorbed surface-active oxygen species (O_2^- , O^-) related to the catalytic performance in oxidation reaction. These results are consistent with the analysis of XPS and $\text{H}_2\text{-TPR}$.

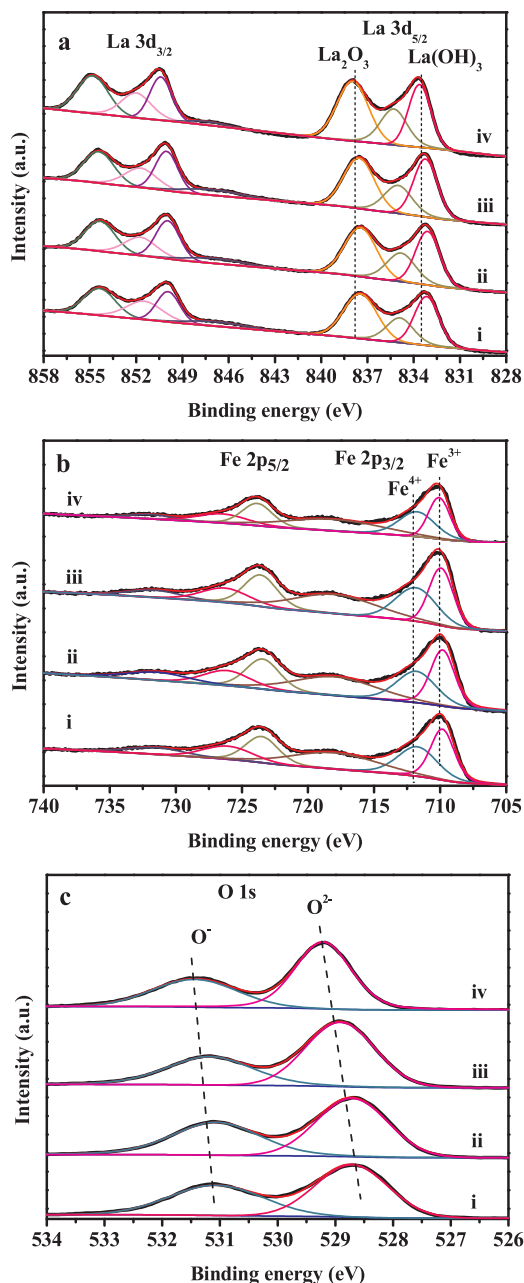


Fig. 4. XPS spectra of La 3d (a), Fe 2p (b) and O 1s (c) regions for $\text{La}_{1-x}\text{K}_x\text{FeO}_{3-\delta}$ nanotubes ((i): $x = 0.3$, (ii): $x = 0.2$, (iii): $x = 0.1$, (iv): $x = 0$).

Table 1

Binding energy (eV) and relative percentages of O_{ads} to O_{lat} .

$\text{La}_{1-x}\text{K}_x\text{FeO}_{3-\delta}$ Catalysts	O_{ads}		O_{lat}		$\text{O}_{\text{ads}}/\text{O}_{\text{lat}}$
	BE(eV)	Area	BE(eV)	Area	
$x = 0$	531.44	27561.77	529.21	48155.13	0.57
$x = 0.1$	531.17	31121.37	528.91	52030.61	0.60
$x = 0.2$	531.06	36775.23	528.71	48598.28	0.76
$x = 0.3$	531.06	33264.23	528.71	44282.01	0.75

3.2. Analysis of the macro/mesoporous nanotube

3.2.1. Analysis of the formation mechanism

Fig. 6 shows the formation process of hollow structure in the prepared catalysts. During the calcination process, some nitrates

decompose into metal oxides after the complete decomposition of PVP at the surface region in the first place, which lead to solid-liquid phase separation. Phase separation is one of the key factors in forming hollow structure. In addition, the DMF as a solvent used in electrospun nitrates/PVP fibers also plays an essential role in the phase separation. DMF has a slow evaporation rate due to the boiling point of 153 °C. It may slow down the solidification of the nitrates/PVP fibers which can contribute to a higher tendency for phase separation. When calcined in the muffle furnace, continuous evaporation and decomposition of DMF will reduce the temperature in the mixture. Meanwhile, the number of degrees of freedom will decrease with the formation of the metal oxides on the surface and the conversion of nitrates to oxides is an endothermic process, thus, the enthalpy of the mixture increases. These changes will bring about increase in the change of Gibbs free energy of the mixture, which can generate the thermodynamic driving force for phase separation [42,43].

While solid-liquid phase separation is formed, the massive nitrates precursors are in the core which can form a concentration gradient simultaneously. It can create a Kirkendall effect [44], which relates to the diffusion of compounds in a sphere with different diffusion rates [45]. The outward transport of nitrates precursor molecules move through the oxide layer quickly. For the balance, the inward flows of vacancies cross to the vicinity of nitrates precursor and nitrates precursor/metal oxides mixture interface. The vacancies are caused by the decomposition of PVP which can assist the exchange of materials by the way of bulk inter-diffusion. Then, the voids transfer the inward flow of vacancies like sinks and the voids can merge into bigger ones. Meanwhile, the new bridges as fast transport paths are built for the remaining nitrates precursor. At this stage, the dominant materials transport process mainly controlled by surface diffusion because the activation energy of the porous surface is much lower than those of bulk diffusion [46]. As a result, metal oxides keep in the shell and the vacancies are continuously formed and flow inward to generate a hollow core. At last, the metal oxides convert to perovskite at high temperature. Therefore, the Kirkendall effect contributes to form hollow structure.

3.2.2. Analysis of the hierarchical macro/mesoporous nanotube structure

To demonstrate the existence of small pores and understand the pore structure properties, Brunauer-Emmett-Teller (BET) surface area and Barrett, Joyner and Halenda (BJH) pore size distributions were determined from the N_2 adsorption-desorption isotherms and shown in Figs. 7, S6 and S7. It can be observed in Fig. 7a that the two samples both exhibit type II isotherms and H3 hysteresis loops in the relative pressure (P/P_0) range from 0.9 to 1 as well as a small H2 type hysteresis loop in the p/p_0 range of 0.2–0.9. As seen, the middle section of the isotherm of $\text{La}_{0.8}\text{K}_{0.2}\text{FeO}_{3-\delta}$ nanotubes at the low-pressure portion is linear, ascribable to the unrestricted mono- or multilayer adsorption, indicates that the sample possesses macroporous structures [38], and the $\text{La}_{0.8}\text{K}_{0.2}\text{FeO}_{3-\delta}$ nanotubes sample get a big rise in adsorption volume at elevated relative pressure, which is the characteristic of textural mesopores or nanovoids existing within the macropore walls [47,48]. The appearance of a small H2-type hysteresis loop in the p/p_0 range of 0.2–0.9 of each sample also suggests the formation of mesopores or nanovoids [49]. These results are supported by the broad pore size distribution of the $\text{La}_{0.8}\text{K}_{0.2}\text{FeO}_{3-\delta}$ nanotubes, which implies that the catalyst possesses macropores and mesopores corresponding to the two peaks at 30–40 nm and 60–70 nm respectively, and larger amount of macropores is obviously obtained by $\text{La}_{0.8}\text{K}_{0.2}\text{FeO}_{3-\delta}$ nanotubes compared with the $\text{La}_{0.8}\text{K}_{0.2}\text{FeO}_{3-\delta}$ bulks, as shown in Fig. 7b. The Brunauer-Emmett-Teller (BET) specific surface area is $18.6 \text{ m}^2 \text{ g}^{-1}$, which is much larger than $\text{La}_{0.8}\text{K}_{0.2}\text{FeO}_{3-\delta}$ bulks samples prepared by traditional methods compared on the basis of the values in Table 3.

The transmission electron microscopy was used to further present the porous tubular morphology, the typical surface pores were marked with yellow arrows and the inner diameter of a nanotube with random selection was marked at around 145 nm which was in the range of inner

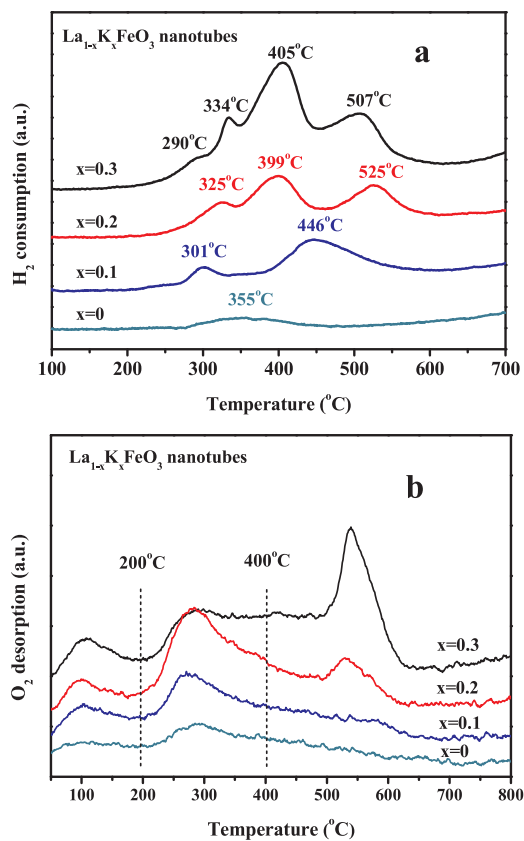


Fig. 5. (a) H_2 -TPR profiles of $La_{1-x}K_xFeO_{38}$ nanotubes ($x = 0, 0.1, 0.2$ and 0.3); (b) O_2 -TPD profiles of $La_{1-x}K_xFeO_{3-δ}$ nanotubes ($x = 0, 0.1, 0.2$ and 0.3).

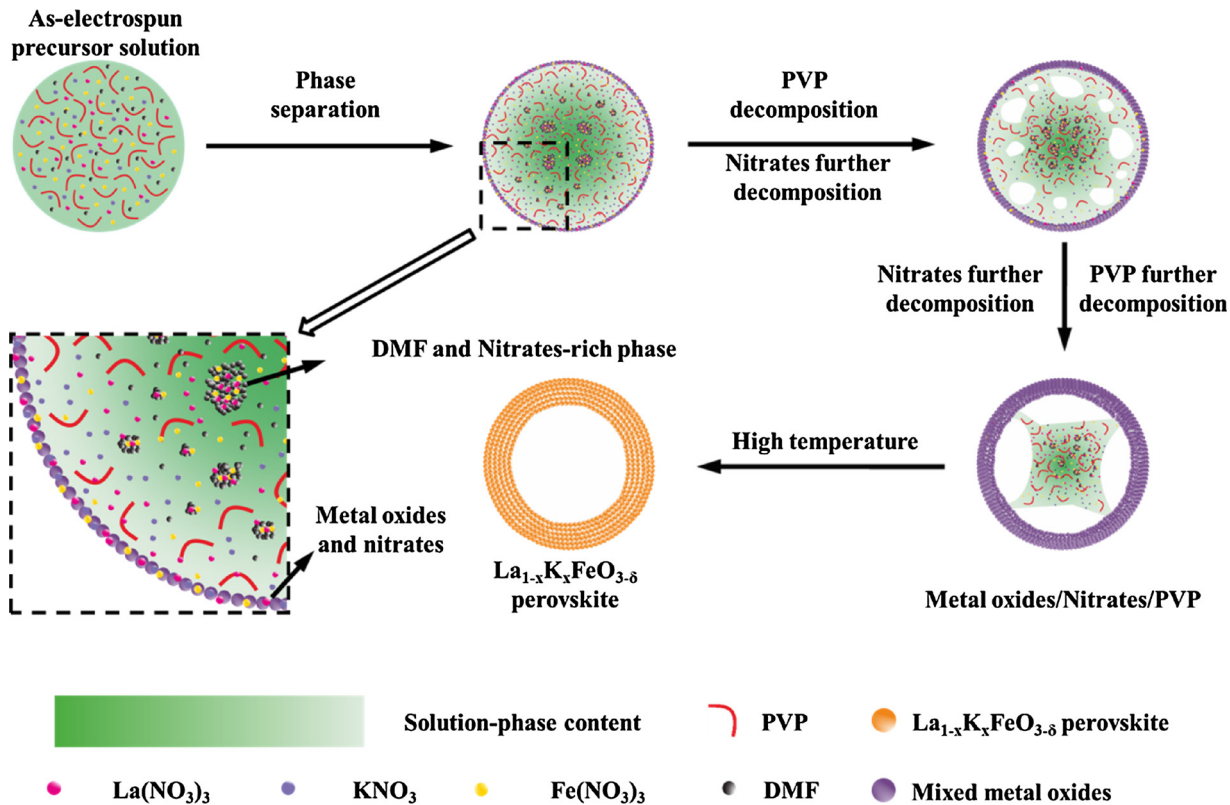


Fig. 6. Schematic illustration of the formation processes of hollow structure.

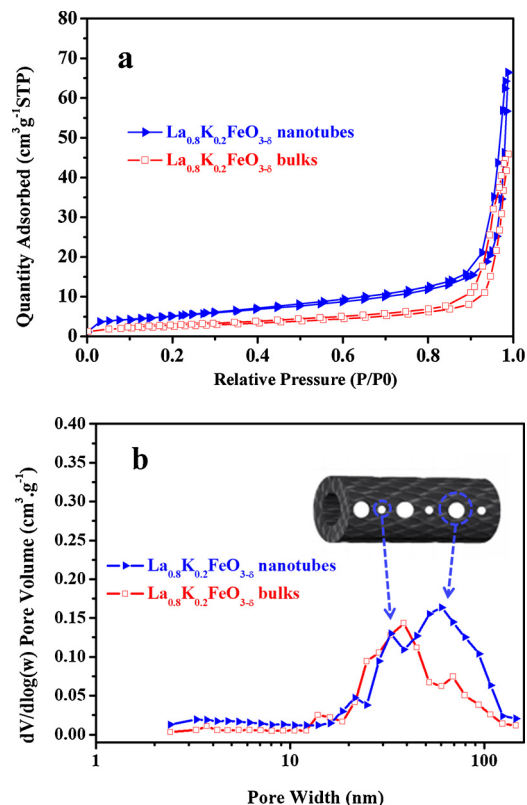


Fig. 7. (a) N_2 adsorption-desorption isotherms of $La_{0.8}K_{0.2}FeO_{3-δ}$ nanotubes and $La_{0.8}K_{0.2}FeO_{3-δ}$ bulks; (b) Pore size distribution of $La_{0.8}K_{0.2}FeO_{3-δ}$ nanotubes and $La_{0.8}K_{0.2}FeO_{3-δ}$ bulks obtained from BJH measurements.

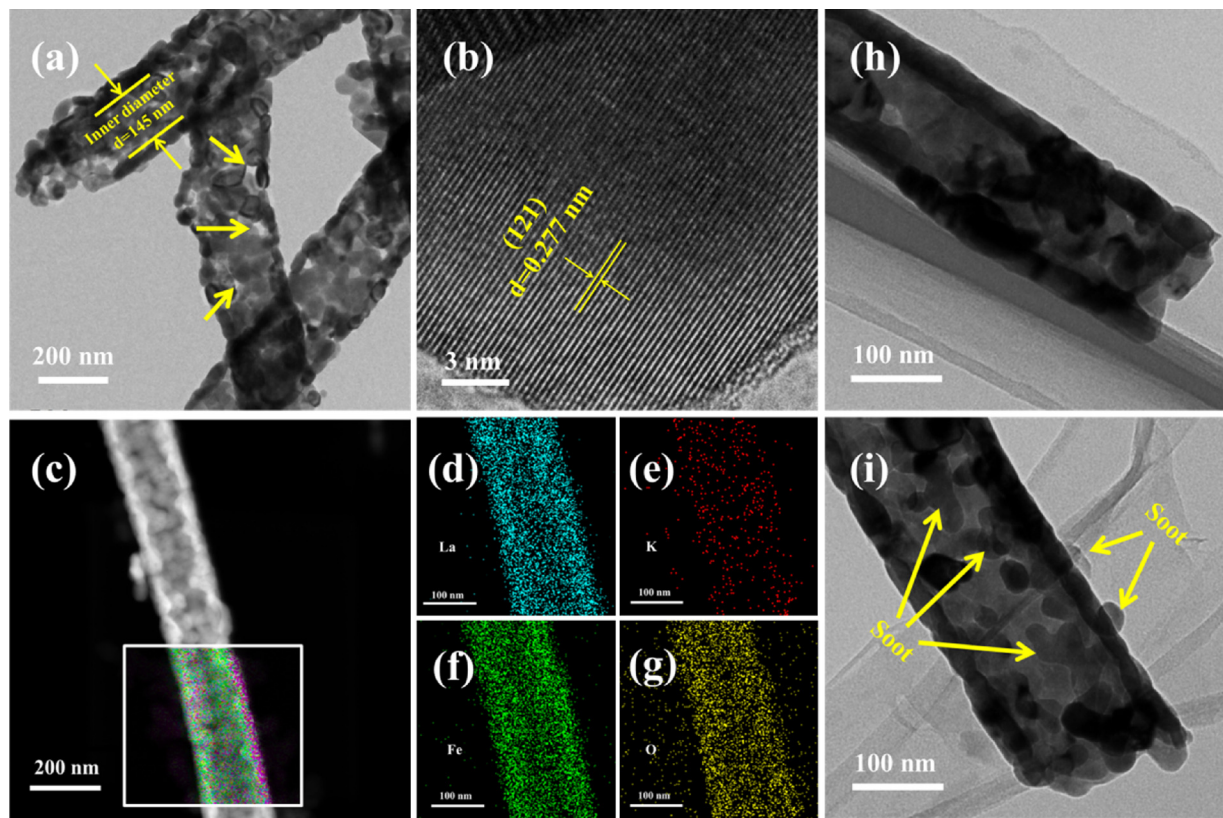


Fig. 8. (a) and (h) TEM images and (b) HRTEM image of $\text{La}_{0.8}\text{K}_{0.2}\text{FeO}_{3-\delta}$ nanotubes; (d–g) EDS elemental mappings (lanthanum (La), potassium (K), iron (Fe), and oxygen (O)) of the area in (c); (i) TEM image of $\text{La}_{0.8}\text{K}_{0.2}\text{FeO}_{3-\delta}$ nanotubes + soot.

diameter distribution (Fig. 8a). These results can further prove the presence of porous structure in the catalyst. Moreover, the TEM images also show the $\text{La}_{0.8}\text{K}_{0.2}\text{FeO}_{3-\delta}$ nanotubes are constituted by various nanoparticles, which indicates that the size of nanoparticles is a key parameter in the nanotubes structure consistent with the discussion about Fig. S5 above. Meanwhile, the high-resolution TEM (HRTEM) image (Fig. 8b) further confirms the formation of the perovskite structure. The d -spacing of lattice fringes is 0.277 nm corresponding to the (121) planes of the $\text{La}_{0.8}\text{K}_{0.2}\text{FeO}_{3-\delta}$ perovskite, which is in agreement with the XRD patterns reported previously. The TEM image and elemental distribution mappings of a typical $\text{La}_{0.8}\text{K}_{0.2}\text{FeO}_{3-\delta}$ nanotube were characterized by energy-dispersive X-ray spectroscopy (EDS) shown in Fig. 8c–g, all elements (La, K, Fe and O) are homogeneously dispersive in the $\text{La}_{0.8}\text{K}_{0.2}\text{FeO}_{3-\delta}$ nanotube due to the corresponding colors. From the results of materials characterizations, it further proved that the hierarchical macro/mesoporous nanotubular $\text{La}_{0.8}\text{K}_{0.2}\text{FeO}_{3-\delta}$ perovskite catalyst was successfully prepared.

3.3. Soot oxidation activity

The soot oxidation performance of as-prepared catalysts was evaluated by simulating soot combustion with a TPO device build independently using the mixtures of soot and catalysts. Although, TC (tight contact) and LC (loose contact) modes are the general methods for evaluating the soot catalytic oxidation performance, this work is more concerned about the LC mode because of the closer conditions in real filter system. Loose contact was achieved by mixing the catalysts and soot with the quality ratio of 9:1 using a spatula and O_2 (without or with NO) was used as oxidation agent. Perovskite bulks were also successfully prepared for comparison proved by XRD patterns and SEM images shown in Figs. S1 and S2. The experimental results are shown in Figs. 9, S8, and Table 2, include the activities of particle catalysts with the same composition respectively and pure soot for comparison.

In case of soot oxidation with O_2 only, the T_{10} , T_{50} , T_{90} and $S_{\text{co}_2}^m$ of pure soot are 497 °C, 570 °C, 612 °C and 40.0%, and the soot conversion temperatures have the trend of going down for the as-prepared perovskite samples. For the perovskite nanotubes, the T_{50} temperature of $\text{La}_{0.8}\text{Fe}_{0.2}\text{O}_{3-\delta}$ nanotubes reduce by 29 °C compared with $\text{La}_{0.9}\text{K}_{0.1}\text{FeO}_{3-\delta}$ nanotubes, implying the introduction of K^+ is very effective for the soot catalytic oxidation corresponding to the analysis results in XPS, $\text{H}_2\text{-TPR}$ and $\text{O}_2\text{-TPD}$. The amount of adsorbed oxygen species was increased and the reducibility of the catalyst was enhanced with the introduction of K^+ , facilitating the transfer of oxygen species and accelerating the redox circulation helpful to the soot combustion. Moreover, the T_{50} temperature of $\text{La}_{0.8}\text{K}_{0.2}\text{FeO}_{3-\delta}$ nanotubes is lower by 45 °C than $\text{La}_{0.8}\text{K}_{0.2}\text{FeO}_{3-\delta}$ due to the superiority of macro/mesoporous tubular structure. For the structure of $\text{La}_{0.8}\text{K}_{0.2}\text{FeO}_{3-\delta}$ nanotubes catalyst, the size of macropores in the external surface and the average nozzle size (98 nm) shown in Fig. 10c are larger than the average particle size at 45.8 nm, which is obtained from the previous work of our group [50]. When mixing the soot with catalysts, the soot particles can go into the nanotube interior through two pathways of the external surface macropores and the nozzle, shown in Fig. 10a and b. These SEM images confirmed that the soot particles can be catalyzed both in the external and internal surface, which can support more contact areas between soot particles and catalyst. This result can be further confirmed by the TEM image in Fig. 8i compared with Fig. 8h, which proves the existence of soot particles both in the external and internal surface of the catalysts. In addition, the gas flows can enter into the porous nanotube from different directions through the pores which can apply different forces on soot particles. It is similar to the confinement effect in the half-closed tube structure of the ordered TiO_2 nanotubes observed by Ming Meng's group [25]. They proposed a novel domin-confined multiple collision based reaction mechanism to interpret the essence of such a confinement effect. On basis of the mechanism, the entered soot particles can produce the Brownian-like movement in the gas flow which contributes

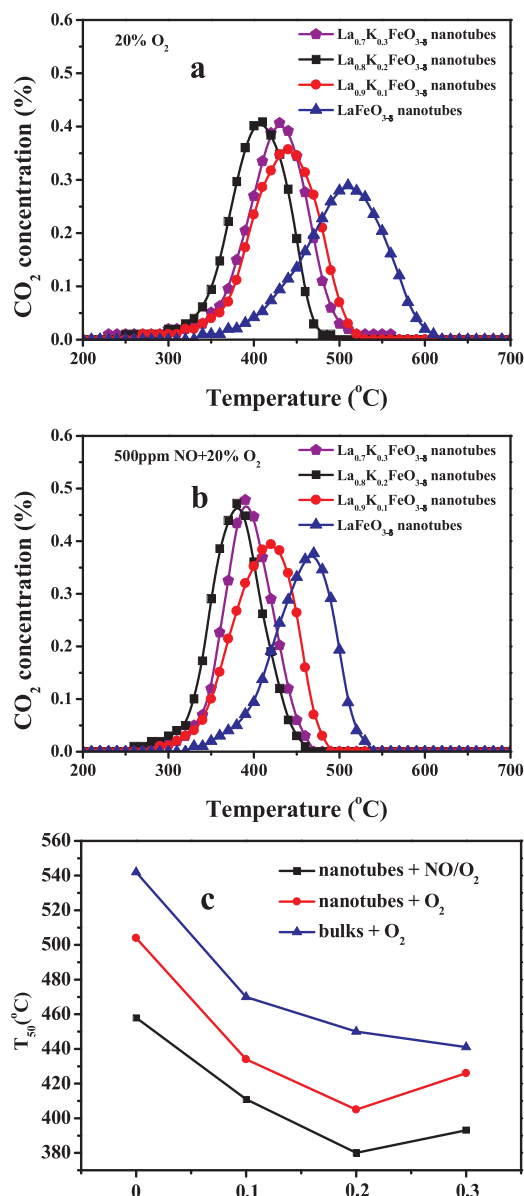


Fig. 9. (a) and (b) CO₂ concentration profiles of soot oxidation over La_{1-x}K_xFeO_{3-δ} nanotubes catalysts under loose contact; (b) The T₅₀ of the La_{1-x}K_xFeO_{3-δ} (x = 0, 0.1, 0.2 and 0.3) nanotubes and bulks catalysts for soot combustion.

to the multiple collisions in the nanotube in this work shown in Fig. 10. As a result, the contact chance between soot particles and catalyst is increased which is favorable to the soot combustion. To sum up, the porous tubular structure employed in soot combustion improves the soot transport capacity and gives more chances to contact between soot and catalyst. When the K-doping amount increases to 30%, the T₅₀ temperature is higher by 21 °C than La_{0.8}K_{0.2}FeO_{3-δ} nanotubes ascribable to the destruction of structure, implying the efficient of porous tubular structure for soot combustion further. On the basis of analysis, it can be gotten that K⁺ and the porous tubular structure are the two key factors for the increase in soot catalytic oxidation in this work. As a result, a small amount of K⁺ introduction is conducive to the formation of tubular structure simultaneously promoting the catalytic performance, while larger amount of K⁺ introduction is contradictory with the presence of the tubular structure. Considering the structural effect and intrinsic properties and based on the lowest temperature at T₅₀ in the presence of O₂ only, the La_{0.8}K_{0.2}FeO_{3-δ} nanotubes catalyst is

Table 2

The temperature and selectivity to CO₂ for soot combustion with or without catalysts.

Catalyst	T ₁₀ (°C)	T ₅₀ (°C)	T ₉₀ (°C)	S _{CO2} ^m (%)
LaFeO _{3-δ} nanotubes	435	504	555	96.9
La _{0.8} K _{0.2} FeO _{3-δ} nanotubes	381	434	479	98.0
La _{0.8} K _{0.2} FeO _{3-δ} nanotubes	358	405	444	95.5
La _{0.7} K _{0.3} FeO _{3-δ} nanotubes	372	426	469	93.4
LaFeO _{3-δ} bulks	465	542	585	100
La _{0.9} K _{0.1} FeO _{3-δ} bulks	416	470	504	99.5
La _{0.8} K _{0.2} FeO _{3-δ} bulks	403	450	479	95.7
La _{0.8} K _{0.3} FeO _{3-δ} bulks	397	441	477	96.4
Pure soot	497	570	612	40.0
LaFeO _{3-δ} nanotubes ^a	406	458	496	92.9
La _{0.8} K _{0.1} FeO _{3-δ} nanotubes ^a	362	411	451	96.5
La _{0.8} K _{0.2} FeO _{3-δ} nanotubes ^a	341	380	418	97.0
La _{0.7} K _{0.3} FeO _{3-δ} nanotubes ^a	355	393	429	94.0

Reaction gas: 20% O₂, 100 ml min⁻¹.

^a Reaction gas: 20% O₂ and 500 ppm NO, 100 ml min⁻¹.

selected as the best candidate for the soot catalytic oxidation in this work while the T₁₀, T₅₀, T₉₀ and S_{CO2}^m are 358 °C, 405 °C, 444 °C and 95.5%. Besides, the soot catalytic combustion experiments were also conducted in 500 ppm NO and 20% O₂, and the results were shown in Fig. 9 and Table 2. By comparison, all the soot conversion temperatures decrease significantly in the presence of NO. As known, NO can be catalytically transformed into NO₂, which has a stronger oxidation ability than O₂. Thus, it can promote the soot conversion with the decrease of T₅₀ temperature [4]. The La_{0.8}K_{0.2}FeO_{3-δ} nanotubes catalyst also shows the highest catalytic activity for soot oxidation in NO/O₂ with its T₅₀ at 380 °C, which is similar to the result in the presence of O₂ only.

For studying the stability of the catalyst, it has been conducted to experience four times TPO test under LC mode after ageing treatment, which was carried out at 700 °C for 4 h under N₂/H₂O mixtures (10 vol % H₂O). The sample after ageing treatment was also characterized by XRD and FESEM methods to study the changes in crystal structure and morphology. It can be seen from Fig. S9a, the two XRD patterns are very close indicating almost no changes at all in crystal structure. Furthermore, Fig. S9b shows the porous tubular structure is preserved and almost same with the fresh sample. The TPO profiles of CO₂ concentration as a function of temperature are shown in Fig. S10. The T₅₀ of aged La_{0.8}K_{0.2}FeO_{3-δ} nanotubes sample is 409 °C, which is close to the T₅₀ of fresh sample. This result proves that the catalyst has a desirable stability. In addition, the aged La_{0.8}K_{0.2}FeO_{3-δ} nanotubes sample has experienced another three times test, and the T₅₀ of sample increases from 409 °C to 410, 412 and 413 °C shown in Table S3. The T₅₀ of aged La_{0.8}K_{0.2}FeO_{3-δ} nanotubes sample has little differences in activity after reused three times. These results indicate that the as-prepared sample is relatively stable. To further investigate the influence of water during the soot combustion reaction, we also have conducted the TPO test in the presence of 6% H₂O. As shown in Fig. S11, the XRD patterns and TPO profiles are almost the same suggesting little effect on the soot catalytic oxidation caused by H₂O.

The isothermal reactions were conducted at 320 °C for 100 min, and the soot conversion of all samples was lower than 15% [30] shown in Fig. S12. As it has been reported, TOF_K is on the basis of K-supporting amount, due to that Mg(Al)-O-K (tightly bound to Mg or Al) and free (isolated) potassium were both catalytically active species which could increase the reactivity and amount of surface active oxygen responsible for the formation of the ketene group [51]. Based on the conclusion, TON_K and TOF_K in this work were on the basis of the K-doping amount which was regarded as the active sites. As calculated in Table 3, the TOF_K values are in the sequence of La_{0.8}K_{0.2}FeO_{3-δ} nanotubes (4.62 × 10⁻⁴ S⁻¹) > La_{0.7}K_{0.3}FeO_{3-δ} nanotubes (3.27 × 10⁻⁴ S⁻¹) > La_{0.8}K_{0.2}FeO_{3-δ} bulks (2.63 × 10⁻⁴ S⁻¹) > La_{0.9}K_{0.1}FeO_{3-δ}

Table 3Specific surface area of various catalysts and the catalytic performances in the soot combustion.^a

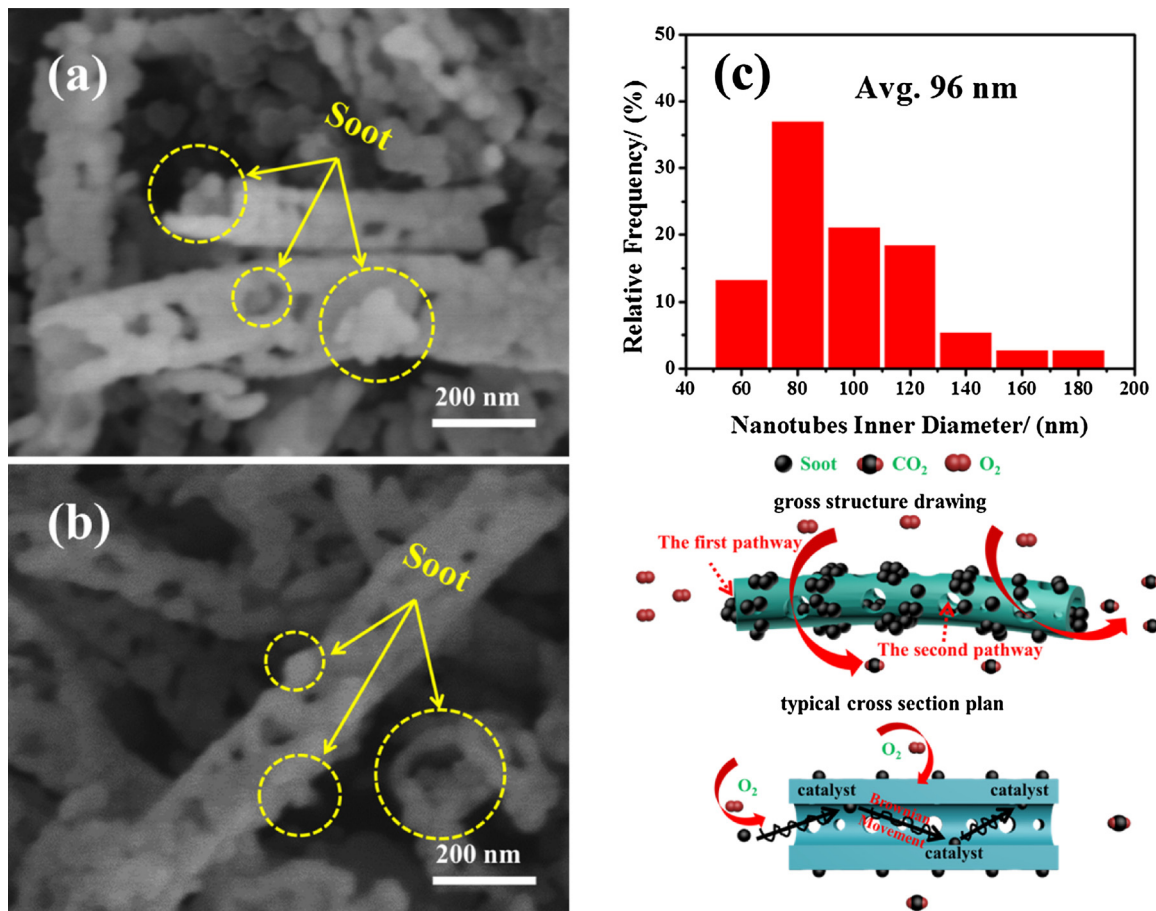
Entry	Catalyst	K content (%) ^b	Conv. (%) ^c	TON _K ^d	TOF _K ^e (S ⁻¹ × 10 ⁻⁴)	Specific surface area (m ² g ⁻¹)
1	La _{0.9} K _{0.1} FeO _{3-δ} nanotubes	1.7	3.5	1.56	2.59	20.1
2	La _{0.8} K _{0.2} FeO _{3-δ} nanotubes	3.5	13.0	2.77	4.62	18.6
3 ^f	La _{0.8} K _{0.2} FeO _{3-δ} nanotubes	3.5	11.4	2.43	4.05	18.6
4	La _{0.8} K _{0.2} FeO _{3-δ} bulks	3.5	7.4	1.58	2.63	9.2
5	La _{0.7} K _{0.3} FeO _{3-δ} nanotubes	5.5	14.4	1.96	3.27	13.2

^a Reaction conditions: 200 mg catalyst with 50 mg soot at 320 °C for 100 min with a 150 ml min⁻¹ gas flow of 20% O₂.^b The weight content of K to total elements (La, K, Fe and O).^c Soot conversion(%) = (mmol CO₂ + mmol CO)/mmol C.^d Turnover number (TON) = (mmol CO₂ + mmol CO)/mmol K.^e Turnover frequency (TOF) = TON/Time.^f Reaction condition: 20% O₂ + 6% H₂O.

nanotubes (2.59×10^{-4} S⁻¹). Meanwhile, the T₁₀ temperatures obtained from the TPO tests are in the sequence of La_{0.8}K_{0.2}FeO_{3-δ} nanotubes (358 °C) < La_{0.7}K_{0.3}FeO_{3-δ} nanotubes (372 °C) < La_{0.9}K_{0.1}FeO_{3-δ} nanotubes (381 °C) < La_{0.8}K_{0.2}FeO_{3-δ} bulks (403 °C). The results of TOF_K calculated are consistent with the TPO tests apart from the La_{0.8}K_{0.2}FeO_{3-δ} bulks compared with La_{0.9}K_{0.1}FeO_{3-δ} nanotubes. The T₁₀ temperature of La_{0.9}K_{0.1}FeO_{3-δ} nanotubes is lower than La_{0.8}K_{0.2}FeO_{3-δ} bulks in TPO tests, showing that La_{0.9}K_{0.1}FeO_{3-δ} nanotubes have the better catalytic activity apparently. However, the TOF_K value of La_{0.9}K_{0.1}FeO_{3-δ} nanotubes is little lower than La_{0.8}K_{0.2}FeO_{3-δ} bulks indicating that the catalytic activity of La_{0.8}K_{0.2}FeO_{3-δ} bulks is better than La_{0.9}K_{0.1}FeO_{3-δ} nanotubes essentially. It is due to that the specific surface area of La_{0.9}K_{0.1}FeO_{3-δ} nanotubes is higher than La_{0.8}K_{0.2}FeO_{3-δ} bulks, which can lead to the exposure of more active sites. Among all

samples, the TOF_K of La_{0.8}K_{0.2}FeO_{3-δ} nanotubes is highest which proves that La_{0.8}K_{0.2}FeO_{3-δ} nanotubes have the most superior catalytic activity. What's more, the TOF_K of La_{0.8}K_{0.2}FeO_{3-δ} nanotubes with 6% H₂O is 4.05×10^{-4} S⁻¹ little lower to the La_{0.8}K_{0.2}FeO_{3-δ} nanotubes with 0% H₂O indicates that it still has a relatively stable catalytic activity in a gas flow with water.

So far, the catalysts with good catalytic activity under the condition of loose contact between catalyst and soot have been reported in the literatures [3–6,10,11,13,14,23,50], shown in Table S4. Compared with these catalysts, the La_{0.8}K_{0.2}FeO_{3-δ} nanotubes catalyst prepared in this work has a desirable catalytic activity for soot oxidation under similar conditions, which can be considered as a good candidate for soot removal.

Fig. 10. FESEM images of La_{0.8}K_{0.2}FeO_{3-δ} nanotubes + soot (a) and (b), and the inner diameter of La_{0.8}K_{0.2}FeO_{3-δ} nanotubes (c).

4. Conclusion

In summary, perovskite-type $\text{La}_{1-x}\text{K}_x\text{FeO}_{3.8}$ nanotubes were successfully fabricated by a simple electrospinning technique following calcination at 700 °C and employed as catalysts for soot removal. The macro/mesoporous nanotubular structure can improve the soot particles transport capacity and increase the contact chance for soot-catalyst. To form the structure, a certain amount of K^+ was introduced into $\text{LaFeO}_{3-\delta}$ which can inhibit the growth of crystallite at a high temperature. Furthermore, the intrinsic properties were also improved with the introduction of K^+ , due to the increase of surface oxygen species and the enhancement of reducibility. However, the excessive introduction amount of K^+ could contribute to the destruction of porous tubular structure which decreases the catalytic activity. Therefore, the catalyst designed should consider both structural effect and intrinsic properties which could promote the catalytic activity more effectively. When the K^+ doping amount increases to 20%, the macro/mesoporous nanotubes catalyst shows the best activity for soot catalytic oxidation with the T_{10} , T_{50} , and T_{90} of 358, 405 and 444 °C, and $S_{\text{CO}_2}^m$ of 95.5% in a gas flow with 20% O_2 . It also shows the best catalytic activity for soot combustion in a gas flow with 20% O_2 and 500 ppm NO. The T_{10} , T_{50} , T_{90} and $S_{\text{CO}_2}^m$ are 341, 380, 418 °C and 97.0%. On the basis of the catalytic performance, the nanotube with the macro/mesoporous structure is meaningful and could be well-referenced for the development of other advanced soot combustion catalysts.

Acknowledgments

The work was supported by the National Key Research and Development Program of China (2016YFC0204301), R&D Project for Environment Protection of Jiangsu of China (NO. 2015002), the Opening Foundation of Jiangsu Key Laboratory of Vehicle Emissions Control (No. OVED031), and the Foundation from State Key Laboratory of Materials-Oriented Chemical Engineering, Nanjing Tech University (ZK201712).

Appendix A. Supplementary data

Supplementary material related to this article can be found, in the online version, at doi:<https://doi.org/10.1016/j.apcatb.2018.05.030>.

References

- [1] H. He, X. Lin, S. Li, Z. Wu, J. Gao, J. Wu, W. Wen, D. Ye, M. Fu, *Appl. Catal. B: Environ.* 223 (2018) 134–142.
- [2] R. Matarrese, S. Morandi, L. Castoldi, P. Villa, L. Lietti, *Appl. Catal. B: Environ.* 201 (2017) 318–330.
- [3] T. Andana, M. Piumetti, S. Bensaid, N. Russo, D. Fino, R. Pirone, *Appl. Catal. B: Environ.* 197 (2016) 125–137.
- [4] Z. Shang, M. Sun, X. Che, W. Wang, L. Wang, X. Cao, W. Zhan, Y. Guo, Y. Guo, G. Lu, *Catal. Sci. Technol.* 7 (2017) 4710–4719.
- [5] L. Cheng, Y. Men, J. Wang, H. Wang, W. An, Y. Wang, Z. Duan, J. Liu, *Appl. Catal. B: Environ.* 204 (2017) 374–384.
- [6] C. Lee, J.I. Park, Y.G. Shul, H. Einaga, Y. Teraoka, *Appl. Catal. B: Environ.* 174–175 (2015) 185–192.
- [7] T. Ryu, N.H. Ahn, S. Seo, J. Cho, H. Kim, D. Jo, G.T. Park, P.S. Kim, C.H. Kim, *E.L. Bruce, Angew. Chem.* 129 (2017) 3304–3308.
- [8] F.E. López-Suárez, M.J. Illán-Gómez, A. Bueno-López, J.A. Anderson, *Appl. Catal. B: Environ.* 104 (2011) 261–267.
- [9] C.V. Preble, T.R. Dallmann, N.M. Kreisberg, S.V. Hering, R.A. Harley, T.W. Kirchstetter, *Environ. Sci. Technol.* 49 (2015) 8864–8871.
- [10] T. Andana, M. Piumetti, S. Bensaid, L. Veyre, C. Thieuleux, N. Russo, D. Fino, E.A. Quadrelli, R. Pirone, *Appl. Catal. B: Environ.* 209 (2017) 295–310.
- [11] C. Cao, L. Xing, Y. Yang, Y. Tian, T. Ding, J. Zhang, T. Hu, L. Zheng, X. Li, *Appl. Catal. B: Environ.* 218 (2017) 32–45.
- [12] L. Castoldi, R. Matarrese, L. Lietti, P. Forzatti, *Appl. Catal. B: Environ.* 90 (2009) 278–285.
- [13] T. Andana, M. Piumetti, S. Bensaid, L. Veyre, C. Thieuleux, N. Russo, D. Fino, E.A. Quadrelli, R. Pirone, *Appl. Catal. B: Environ.* 226 (2018) 147–161.
- [14] J. Wang, G. Yang, L. Cheng, E.W. Shin, Y. Men, *Catal. Sci. Technol.* 5 (2015) 4594–4601.
- [15] H. Liang, Y. Mou, H. Zhang, S. Li, C. Yao, X. Yu, *Catal. Today* 281 (2017) 477–481.
- [16] C. Lee, Y. Jeon, S. Hata, J.I. Park, R. Akiyoshi, H. Saito, Y. Teraoka, Y.G. Shul, H. Einaga, *Appl. Catal. B: Environ.* 191 (2016) 157–164.
- [17] C.H. Kim, G. Qi, K. Dahlberg, W. Li, *Science* 327 (2010) 1624.
- [18] L. Wang, S. Fang, N. Feng, H. Wan, G. Guan, *Chem. Eng. J.* 293 (2016) 68–74.
- [19] H. Zhu, P. Zhang, S. Dai, *ACS Catal.* 5 (2015) 6370–6385.
- [20] A. Eysller, A. Winkler, P. Mandaliev, P. Hug, A. Weidenkaff, D. Ferri, *Appl. Catal. B: Environ.* 106 (2011) 494–502.
- [21] Y.-F. Sun, J.-H. Li, Y.-Q. Zhang, B. Hua, J.-L. Luo, *ACS Catal.* 6 (2016) 2710–2714.
- [22] L. Tang, Z. Zhao, Y. Wei, J. Liu, Y. Peng, K. Li, *Catal. Today* 297 (2017) 131–142.
- [23] Y. Wei, J. Liu, Z. Zhao, Y. Chen, C. Xu, A. Duan, G. Jiang, H. He, *Angew. Chem. Int. Ed.* 50 (2011) 2326–2329.
- [24] Y. Kobayashi, T. Saito, A. Isogai, *Angew. Chem.* 126 (2014) 10562–10565.
- [25] Y. Yu, J. Ren, D. Liu, M. Meng, *ACS Catal.* 4 (2014) 934–941.
- [26] D. Hou, W. Luo, Y. Huang, J.C. Yu, X. Hu, *Nanoscale* 5 (2013) 2028–2035.
- [27] S. An, Y.I. Kim, H.S. Jo, M.-W. Kim, M.W. Lee, A.L. Yarin, S.S. Yoon, *Chem. Eng. J.* 327 (2017) 336–342.
- [28] Y.-J. Chiu, H.-F. Tseng, Y.-C. Lo, B.-H. Wu, J.-T. Chen, *Macromolecules* 50 (2017) 9024–9031.
- [29] Y. Wang, H. Huang, G. Li, X. Zhao, L. Yu, C. Zou, Y. Xu, *CrystEngComm* 19 (2017) 2673–2680.
- [30] Z. Zhang, D. Han, S. Wei, Y. Zhang, *J. Catal.* 276 (2010) 16–23.
- [31] R.F. Cotta, K.A. da Silva Rocha, E.F. Kozhevnikova, I.V. Kozhevnikov, E.V. Gusevskaya, *Appl. Catal. B: Environ.* 217 (2017) 92–99.
- [32] T.M. Suzuki, T. Takayama, S. Sato, A. Iwase, A. Kudo, T. Morikawa, *Appl. Catal. B: Environ.* 224 (2018) 572–578.
- [33] Y. Liu, Y. Zhou, J. Li, Q. Wang, Q. Qin, W. Zhang, H. Asakura, N. Yan, J. Wang, *Appl. Catal. B: Environ.* 209 (2017) 679–688.
- [34] Y.J. Kim, J.K. Lee, K.M. Min, S.B. Hong, I.-S. Nam, B.K. Cho, *J. Catal.* 311 (2014) 447–457.
- [35] N. Escalona, S. Fuentealba, G. Pecchi, *Appl. Catal. A* 381 (2010) 253–260.
- [36] W.Y. Lee, H.J. Yun, J.W. Yoon, *J. Alloys Compd.* 583 (2014) 320–324.
- [37] J. Xu, J. Liu, Z. Zhao, C. Xu, J. Zheng, A. Duan, G. Jiang, *J. Catal.* 282 (2011) 1–12.
- [38] K. Ji, H. Dai, J. Deng, H. Jiang, L. Zhang, H. Zhang, Y. Cao, *Chem. Eng. J.* 214 (2013) 262–271.
- [39] N.A. Merino, B.P. Barbero, P. Grange, L.E. Cadús, *J. Catal.* 231 (2005) 232–244.
- [40] A. Kahoul, A. Hammouche, F. Nâamoune, P. Chartier, G. Poillerat, J.F. Koenig, *Mater. Res. Bull.* 35 (2000) 1955–1966.
- [41] P. Giambelli, S. Cimino, L. Lisi, M. Faticanti, G. Minelli, I. Pettiti, P. Porta, *Appl. Catal. B: Environ.* 33 (2001) 193–203.
- [42] K. Nakanishi, N. Tanaka, *Acc. Chem. Res.* 40 (2007) 863–873.
- [43] C. Triantafyllidis, M.S. Elsaesser, N. Hüsing, *Chem. Soc. Rev.* 42 (2013) 3833–3846.
- [44] W. Wang, M. Dahl, Y. Yin, *Chem. Mater.* 25 (2013) 1179–1189.
- [45] J. Kong, H.R. Tan, S.Y. Tan, F. Li, S.Y. Wong, X. Li, X. Lu, *Chem. Commun.* 46 (2010) 8773–8775.
- [46] H.J. Fan, M. Knez, R. Scholz, D. Hesse, K. Nielsch, M. Zacharias, U. Gösele, *Nano Lett.* 7 (2007) 993–997.
- [47] H. Li, L. Zhang, H. Dai, H. He, *Inorg. Chem.* 48 (2009) 4421–4434.
- [48] X. Wang, X. Zhang, Y. Wang, H. Liu, J. Qiu, J. Wang, W. Han, K.L. Yeung, *Chem. Mater.* 23 (2011) 4469–4479.
- [49] W.-C. Li, A.-H. Lu, C. Weidenthaler, F. Schüth, *Chem. Mater.* 16 (2004) 5676–5681.
- [50] N. Feng, C. Chen, J. Meng, Y. Wu, G. Liu, L. Wang, H. Wan, G. Guan, *Catal. Sci. Technol.* 6 (2016) 7718–7728.
- [51] Z. Zhang, Y. Zhang, Z. Wang, X. Gao, *J. Catal.* 271 (2010) 12–21.